Microspectroscopic imaging of Nodulation factor binding sites on livingVicia sativa roots using a novel fluorescent bioactive Nodulation factor

Gadella, Th.W.J.; Vereb, G.; Hadri, A.-E.; Röhrig, H.; Schmidt, J.; John, M.

DOI
10.1016/S0006-3495(97)78843-X

Publication date
1997

Published in
Biophysical Journal

Microspectroscopic Imaging of Nodulation Factor-Binding Sites on Living *Vicia sativa* Roots Using a Novel Bioactive Fluorescent Nodulation Factor

Theodorus W. J. Gadella, Jr.,* György Vereb, Jr.,# Az-Eddine Hadri,§ Horst Röhrig,¶ Jürgen Schmidt,¶ Michael John,¶ Jeff Schell,¶ and Ton Bisseling§

*Microspectroscopy Center Wageningen, Departments of Molecular Biology and Biochemistry, Wageningen Agricultural University, Dreijenlaan 3, NL-6703 HA Wageningen, The Netherlands; #Department of Molecular Biology, Max Planck Institute for Biophysical Chemistry, Göttingen, Germany; §Department of Molecular Biology, Wageningen Agricultural University, Wageningen, The Netherlands; and ¶Abteilung Genetische Grundlagen der Pflanzenzüchtung, Max-Planck-Institut für Züchtungsforschung, Cologne, Germany

ABSTRACT A novel bioactive fluorescent nodulation (Nod) factor, NodRlv-IV(BODIPY FL-C_{16}), has been synthesized by attaching a BODIPY FL-C_{16} acyl chain to the primary amino group of chitotetraose deacetylated at the nonreducing terminus by recombinant NodB. The binding of the fluorescent Nod factor to root systems of *Vicia sativa* was investigated with fluorescence spectral imaging microscopy (FSPIM) and fluorescence ratio imaging microscopy (FRIM). Spatially resolved fluorescence spectra of living and labeled *Vicia sativa* root systems were measured by FSPIM. Strong autofluorescence, inherent to many plant systems when excited at 488 nm, was corrected for by utilizing the difference in fluorescence emission spectra of the autofluorescence and NodRlv-IV(BODIPY FL-C_{16}). A methodology is presented to break down the in situ fluorescence emission spectra into spatially resolved autofluorescence and BODIPY FL fluorescence spectra. Furthermore, an FRIM method was developed for correcting autofluorescence in fluorescence micrographs for this system. After autofluorescence correction it was shown that NodRlv-IV(BODIPY FL-C_{16}) was concentrated in the root hairs, but was also bound to other parts of the root surface.

INTRODUCTION

Root systems of legumes are capable of reducing atmospheric N_2, converting it to ammonium. This process is localized in small root nodules that are formed by a symbiosis with *Rhizobium* bacteria. The first visible step in the formation of root nodules is the deformation and curling of root hairs. Furthermore, nodule primordia are formed in the root cortex that differentiate to root nodules, as is described in detail elsewhere (Heidstra and Bisseling, 1996; Nap and Bisseling, 1990).

Root hair deformation and primordium formation are induced by lipochitooligosaccharides (LCOs) that are secreted by the *Rhizobium* bacterium. These LCOs, also called nodulation (Nod) factors, consist of a tetramer or pentamer of *N*-acetyl-glucosamine and an acyl chain attached to the nonreducing sugar residue (Dénarié and Cullimore, 1993; Fisher and Long, 1992; Mylona et al., 1994; Spaink, 1992; Vijn et al., 1995). Purified Nod factors are active in concentrations as low as 10^{-12} M (Dénarié and Cullimore, 1993; Spaink, 1992). Because of the important role of Nod factors as plant growth regulators, different methods for the synthesis of these signaling molecules have been developed (Nicolaou et al., 1992; Röhrig et al., 1995, 1996).

Received for publication 20 September 1996 and in final form 28 January 1997.

Address reprint requests to Dr. T. W. J. Gadella, Jr., Microspectroscopy Center, Wageningen, Department of Molecular Biology, Wageningen Agricultural University, Dreijenlaan 3, NL-6703 HA Wageningen, The Netherlands. Tel.: +31-317-484284; Fax: +31-317-483584; E-mail: dorus.gadella@laser.bc.wau.nl.

0006-3495/97/05/1986/11 $2.00

Heidstra et al. have developed a root hair deformation assay for *Vicia sativa*, in which purified Nod factors can induce root hair deformation in a spatially and temporally controlled way (Heidstra et al., 1994). Within 3 h of adding Nod factor to *Vicia* roots, root hair deformation is clearly visible in a narrow zone of the root, called the susceptible zone. This zone is about 2 mm long and contains the root hairs that just have reached their mature size, but does not include young elongating hairs or full-grown mature root hairs. The susceptible and nonsusceptible zones can be distinguished using Nomarski optics, for the growing hairs have a polarly organized cytoplasm that results in a so-called clear zone at the tip.

It has been shown recently that calcium spiking with a periodicity of about 60 s is induced after application of Nod factors to alfalfa root hairs (Ehrhardt et al., 1996). This suggests that intracellular signal transduction by the phosphoinositide cascade is triggered by Nod factors (Divecha and Irvine, 1995).

To gain more insight in the mechanism by which Nod factors are perceived by the plant, we labeled a Nod factor with a fluorescent tag and studied the localization of the fluorescent Nod factor on living *Vicia* roots. Because of extensive autofluorescence, standard fluorescence microscopy proved unsuitable for visualization of the in vivo binding sites on root systems. In this paper we describe a methodology for overcoming this problem. These techniques exploit the emission spectral properties of the labeled root system. The difference in the spectral distribution of autofluorescence and the labeled Nod factor can be utilized to achieve contrast.

The spectral dependence of fluorescence emission or excitation has been employed previously to image cellular

parameters such as $[Ca^{2+}]_i$ or pH (Bright et al., 1989; Giuliano et al., 1990; Waggoner et al., 1989). Moreover, other spectroscopic modalities have been implemented in the microscope to achieve contrast, such as fluorescence spectroscopy (Balaban et al., 1985; Martinez-Zaguilan et al., 1994; Trepte et al., 1994), fluorescence anisotropy (Burghardt and Ajtai, 1991; Dix and Verkman, 1990; Florine-Casteel et al., 1990), dichroism (Beach et al., 1987; Kim et al., 1987; Mickols et al., 1985), fluorescence resonance energy transfer (FRET) (Herman, 1989; Jovin and Arndt-Jovin, 1989a), photobleaching kinetics (Arndt-Jovin et al., 1979; Gadella and Jovin, 1995), fluorescence lifetimes (Buurman et al., 1992; Gadella et al., 1993; Lakowicz, 1994), and delayed luminescence (Beverloo et al., 1992; Marriott et al., 1991, 1994). One key element common to all of these diverse imaging systems is the coupling to digital imaging detectors. Scientific slow-scan CCD cameras with high sensitivity and dynamic range (Aikens et al., 1989) enable the capturing of high-resolution digital images that can be post-processed to extract quantitative information (Herman and Jacobson, 1990; Jovin and Arndt-Jovin, 1989b).

Using fluorescence ratio imaging microscopy (FRIM) and fluorescence spectral imaging microscopy (FSPIM), we were able to effectively suppress autofluorescence in the image, even when it accounted for as much as 90% of the steady fluorescence state emission signal. As a consequence, it will be possible to study the spatial distribution of Nod factor-binding sites on living *Vicia* roots. The methodology is not restricted to this plant system, but may be applied generally to any biological specimen.

MATERIALS AND METHODS

Synthesis of NodRlv-IV(BODIPY FL-C_{16})

Chitotetraose (Seikagaku, Japan) was deacetylated at the nonreducing GlcNAc residue by recombinant NodB (John et al., 1993). The resulting Glc*N* (β 1–4 GlcNAc)$_3$ backbone was purified by cation exchange chromatography as described previously (Röhrig et al., 1994). One milligram of 4,4-difluoro-5,7-dimethyl-4-bora-3a,4a-diaza-*s*-indacene-3-hexadecanoic acid (BODIPY FL-C_{16}; Molecular Probes Europe, Leiden, The Netherlands) was dissolved in acetonitrile (100 μl) and treated with triethylamine (0.7 μl; ICN, Eschwege, Germany) and 2-chloro-1-methylpyridinium iodide (1 mg, Sigma) for 15 min at 30°C under argon. For *N*-acylation of the free amino group of the tetrasaccharide backbone, a solution of carbohydrate (1.2 mg) in dimethylsulfoxide (200 μl) was added to the reaction mixture under stirring. The mixture was stirred for 2 h at 30°C under argon. The fluorescent Nod factor NodRlv-IV (BODIPY FL-C_{16}; see Fig. 1 *A*) was isolated by high-performance liquid chromatography (HPLC) purification on a preparative C_{18} reversed-phase column (1.0 cm × 25 cm, Ultrasphere ODS; Beckman) using a 30-min linear acetonitrile gradient (30–80%). The HPLC was connected to a variable-wavelength detector and a fluorescence monitor.

Plant culture conditions and root hair deformation assay

Seeds of *Vicia sativa*, subspecies nigra, were germinated and grown in modified Fåhraeus slides (Bhuvaneswari and Solheim, 1985) as described

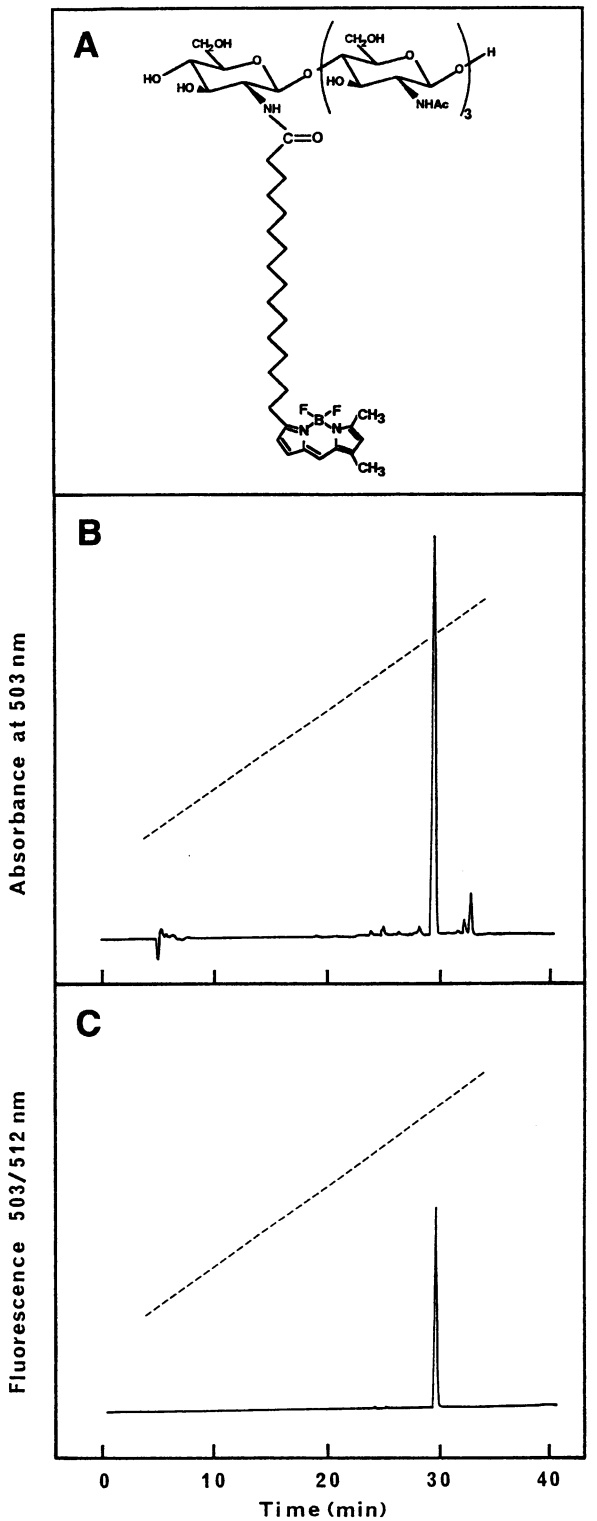

FIGURE 1 Purification of NodRlv-IV (BODIPY FL-C_{16}) by reversed-phase HPLC. (*A*) Structure of NodRlv-IV (BODIPY FL-C_{16}). (*B*) Synthetic fluorescent Nod factor was separated on a C_{18} reversed-phase column and eluted with a linear acetonitrile gradient (30–80%, *broken line*) at a flow rate of 2.0 ml/min. Elution profile of NodRlv-IV (BODIPY FL-C_{16}) was monitored at 503 nm. (*C*) Rechromatography of purified NodRlv-IV (BODIPY FL-C_{16}). Chromatographic conditions were the same as in *B*. Column effluent was monitored by a fluorescence detector (λ_{ex} = 503 nm, λ_{em} = 512 nm).

earlier (Heidstra et al., 1994; Van Brussel et al., 1982). *Vicia sativa* root hair deformation was investigated 5 days after germination of the seeds in Fåhraeus slides as described (Heidstra et al., 1994).

Fluorescence spectroscopy

Twelve susceptible zones of *Vicia* roots incubated with NodRlv-IV(BODIPY FL-C_{16}) were cut out and frozen in liquid nitrogen. After grinding they were suspended in 1 ml of Fåhraeus medium (Fåhraeus, 1957). A control was made by giving unlabeled susceptible zones the same treatment. After dilution to 3 ml and pipeting into a 3-ml quartz fluorescence cuvette, fluorescence spectra were taken of the turbid solutions. The spectra were measured at 25°C using an SPF-500C spectrofluorimeter (SLM Instruments, Urbana, IL). The excitation wavelength was 470 nm (slit 4 nm) and was passed through a 469.9-nm HW, 12.2-nm narrow bandpass filter (no. 74921.3; Schott, Mainz, Germany) to remove residual excitation light at higher wavelengths that was found to interfere with the fluorescence spectra because of substantial scattering in the turbid homogenized samples. Emission spectra were recorded from 500 to 700 nm (slit 2.5 nm), the background fluorescence of the Fåhraeus medium was subtracted, and the resulting difference spectrum was corrected for the instrument response characteristics.

Fluorescence spectral imaging microscopy

Spectral imaging was done using a Zeiss Axioplan microscope with double TV module (Zeiss, Oberkochen, Germany). Epifluorescence illumination was provided with a 50-W mercury lamp. A 475DF30 bandpass excitation filter, a 500DCLP dichroic mirror (Omega, Brattleboro, VT), and a OG515 longpass emission filter (Schott) were used. The specimens were observed with a 10× Plan Neofluar (NA 0.3) objective.

Emission spectra were resolved with a SpectraPro-150 dual-grating stigmatic imaging monochromator (Acton Research Corp., Acton, MA). The operation of the equipment is described in detail elsewhere (Vereb and Jovin, manuscript in preparation). The data presented were obtained with a grating of 300 lines/mm. The central wavelength was selected via serial port communication from the Macintosh Quadra 800 computer. Phase contrast and fluorescence images without spectral resolution were taken with the input slit opened to 3 mm, and the grating set to a 0-nm central wavelength (nondispersive mode). A further image was taken in the nondispersive mode after setting the entrance slit to 50 μm, to identify the columns of image pixels, the spectra of which were then taken.

Spectra were taken at 50-μm slit width, 590-nm central wavelength. An SBIG (Santa Barbara Instruments Group, Santa Barbara, CA) ST-6 imaging CCD camera was used to acquire spectral images, containing the original vertical spatial information of the imaged strip in one dimension, and spectra in the other. Exposure time was 15 s for all spectra. A 3 × 2 binning was used on the 750 × 242 (23 μm wide × 27 μm) pixel chip, which was cooled thermoelectrically to −30°C. Data were digitized at 16-bit resolution and read to the Quadra computer via a serial port using the program KestrelSpec (RHEA Corp., Wilmington, DE). Spectra were calibrated using defined mercury lines.

Conventional fluorescence images of the same specimen were taken with a Photometrics (Tucson, AR) series 200 cooled slow scan CCD camera equipped with a Kodak KAF-1400 chip, interfaced to a Macintosh Quadra 800 computer (Apple Computer, Cupertino, CA).

The spectral fitting has been implemented in a custom-written routine in C language that has been attached to the commercial image-processing package SCIL-Image (TPD, Delft, The Netherlands), which is implemented on a powerful Silicon Graphics Inc. (SGI) Indy workstation.

Fluorescence ratio imaging microscopy

The FRIM system consisted of 1) an Innova 70 Ar/Kr mixed-gas laser (Coherent, Santa Clara, CA) as the excitation source; 2) a Leica DMR-RBE fluorescence microscope (Leitz, Wetzlar, Germany) incorporating a Leitz Fluotar 10×, NA 0.3 air objective, a 505-nm dichroic mirror, and a D525/20 (λ_1) or D580/40 (λ_2) emission filter (Chroma Technology, Brattleboro, VT); and 3) a slow-scan series 200 (CH250) CCD camera system (Photometrics). The CCD camera system incorporated 1) a SI 502/AB grade 1 thinned and back-illuminated CCD sensor with multiphase pinning (MPP) containing 510 × 510 (available) square 24-μm pixels, with a full well capacity of 376 ke^-, a dark current of 0.87 e^-/s at −40°C, and a quantum yield of up to 80%; 2) a liquid cooling circulator (LCU220) permitting standard cooling of the chip down to −40°C; 3) a CE200a camera control unit with a built-in 14-bit (0–16383) analog-to-digital converter operating at 200 kHz; 4) a Nu200 interface card inserted into a Nubus slot of an Apple Macintosh PowerPC 7100/66 computer; and 5) camera control software implemented within the IPLab 3.0 program (Signal Analytics, Vienna, VA). Images were taken of the susceptible zone of *Vicia sativa* roots by 5-s exposure to the 488-nm excitation light and simultaneous integration of the fluorescence signal on the CCD (no binning).

THEORY

Autofluorescence correction in spectral imaging microscopy

By means of spectral fitting it is possible to resolve a mixed spectrum into its individual spectral components, provided that the spectra of the individual components are known from another experiment. Thus, in addition to an image spectrum of a probe-labeled and autofluorescing biological sample (designated $S_L(\lambda, x)$ in Eq. 1), a fluorescence spectrum of the probe in solution (designated $S_P(\lambda)$) and of an unlabeled biological sample (designated $S_A(\lambda)$) are required. All the of spectra have to be corrected for background (e.g., buffer) contributions and electronic effects (see below) by subtraction before spectral fitting.

$$S_L(\lambda, x) = \alpha(x) \cdot S_A(\lambda) + \beta(x) \cdot S_P(\lambda). \quad (1)$$

In Eq. 1, $\alpha(x)$ and $\beta(x)$ represent the spatial distribution (in one dimension) of the relative contributions of autofluorescence and probe fluorescence in the specimen. One can use the averaged image spectra (over distance) of an unlabeled (autofluorescing) sample and that of a probe solution for the fit. Averaging within the unlabeled sample requires prior confirmation that the autofluorescence spectrum is not dependent on the spatial localization x. Equation 1 is linear with respect to $\alpha(x)$ and $\beta(x)$, so one can use a linear least-squares algorithm (Draper and Smith, 1981) to fit the spatial distributions $\alpha(x)$ and $\beta(x)$ that best satisfy Eq. 1:

$$\begin{bmatrix}\alpha(x)\\ \beta(x)\end{bmatrix} = \begin{bmatrix}\sum_\lambda S_A^2(\lambda) & \sum_\lambda S_A(\lambda)\cdot S_P(\lambda)\\ \sum_\lambda S_A(\lambda)\cdot S_P(\lambda) & \sum_\lambda S_P^2(\lambda)\end{bmatrix}^{-1} \begin{bmatrix}\sum_\lambda S_A(\lambda)\cdot S_L(\lambda, x)\\ \sum_\lambda S_P(\lambda)\cdot S_L(\lambda, x)\end{bmatrix}. \quad (2)$$

Correction for autofluorescence by fluorescence ratio imaging microscopy

To correct for autofluorescence in a fluorescence micrograph of a labeled specimen ($F_{L,\lambda}(x, y)$), one needs images

of three additional specimens: an unlabeled specimen ($F_{U,\lambda}(x, y)$), a probe solution on a microscope slide ($F_{P,\lambda}(x, y)$), and a blank slide containing the labeling buffer ($F_{B,\lambda}(x, y)$), taken with identical optics and exposure times. The x, y coordinates indicate the spatial dependence of fluorescence at each position (pixel) in the image. All images should be taken at two different excitation or emission wavelengths. The latter three pairs of images must be taken only once and can be used for the correction of more ($F_{L,\lambda}(x, y)$) images. As described in Eq. 3, the fluorescence intensity in the images depends on the spatial distribution of the excitation light intensity in the object plane (designated by ($E_\lambda(x, y)$)), the spatial distribution of the fluorescent probe ($P(x, y)$), its apparent fluorescence quantum yield ($Q_{P,\lambda}$), the distribution of autofluorescing molecules ($A(x, y)$), with corresponding quantum yield $Q_{A,\lambda}$ and a background term designated $F_{B,\lambda}(x, y)$:

$$\begin{cases} F_{P,\lambda}(x, y) = E_\lambda(x, y) \cdot P_P(x, y) \cdot Q_{PS,\lambda} + F_{B,\lambda}(x, y) \\ \qquad\qquad = \alpha \cdot E_\lambda(x, y) \cdot Q_{P,\lambda} + F_{B,\lambda}(x, y) \\ F_{U,\lambda}(x, y) = E_\lambda(x, y) \cdot A_U(x, y) \cdot Q_{A,\lambda} + F_{B,\lambda}(x, y) \\ F_{L,\lambda}(x, y) = E_\lambda(x, y) \cdot (A_L(x, y) \cdot Q_{A,\lambda} + P_L(x, y) \cdot Q_{P,\lambda}) \\ \qquad\qquad + F_{B,\lambda}(x, y) \\ F_{B,\lambda}(x, y) = E_\lambda(x, y) \cdot B(x, y) \cdot Q_{B,\lambda} + \text{Bias}. \end{cases} \tag{3a,b,c,d}$$

In general, the quantum yields of the probe in solution ($Q_{PS,\lambda}$) and in a biological specimen ($Q_{P,\lambda}$) will differ. $Q_{PS,\lambda}$ depends on the absorption cross section of the probe (see Jovin and Arndt-Jovin, 1989b; Jovin et al., 1990), the characteristics of the excitation and emission filters, the sensitivity of the CCD camera, and the true fluorescence quantum yield of the probe (Jovin and Arndt-Jovin, 1989b). The "background" fluorescence images $F_{B,\lambda}(x, y)$ are usually determined mainly by the electronic CCD camera bias and dark current, but can be larger in the case of leakage of a very small amount of excitation light through the emission filters or by fluorescence generated by the microscope optics.

In Eq. 3a it is assumed that the probe is distributed homogeneously in the solution. Hence $P_P(x, y) \cdot Q_{PS,\lambda}$ can be substituted for $\alpha Q_{P,\lambda}$, where α is proportional to the concentration of the probe in the solution. Another essential assumption is that the ratio of autofluorescence intensity at the two applied wavelengths should be similar for all pixels.

We define two sets of ratio images ($R_{L,\lambda}(x, y)$ and $R_{U,\lambda}(x, y)$) in Eqs. 4 and 5 by background correction of $F_{L,\lambda}(x, y)$ and $F_{U,\lambda}(x, y)$, respectively, and normalizing to the probe fluorescence. This procedure also results in flat-field correction (Jericevic et al., 1989):

$$R_{L,\lambda}(x, y) \equiv \frac{F_{L,\lambda}(x, y) - F_{B,\lambda}(x, y)}{F_{P,\lambda}(x, y) - F_{B,\lambda}(x, y)} = \frac{1}{\alpha} \cdot \left(A_L(x, y) \frac{Q_{A,\lambda}}{Q_{P,\lambda}} + P_L(x, y) \right) \tag{4}$$

$$R_{U,\lambda}(x, y) \equiv \frac{F_{U,\lambda}(x, y) - F_{B,\lambda}(x, y)}{F_{P,\lambda}(x, y) - F_{B,\lambda}(x, y)} = \frac{1}{\alpha} \cdot \left(A_U(x, y) \frac{Q_{A,\lambda}}{Q_{P,\lambda}} \right). \tag{5}$$

From the pair of $R_{U,\lambda}(x, y)$ ratio images (Eq. 5), the important constant R is defined in Eq. 6. This definition of R renders an image rather than a constant, so that one can check the last assumption of the constant autofluorescence quantum yield ratio:

$$R \equiv \frac{R_{U,\lambda_1}(x, y)}{R_{U,\lambda_2}(x, y)} = \left(\frac{Q_{A,\lambda_1}}{Q_{P,\lambda_1}} \right) \Big/ \left(\frac{Q_{A,\lambda_2}}{Q_{P,\lambda_2}} \right) \quad \text{or} \quad \frac{Q_{A,\lambda_1}}{Q_{P,\lambda_1}} = R \cdot \frac{Q_{A,\lambda_2}}{Q_{P,\lambda_2}}. \tag{6}$$

By combination of Eqs. 4 and 6 one can construct quantitative images representing the probe and autofluorescence distribution in the labeled specimen according to Eqs. 7 and 8, respectively. Both images are corrected for background fluorescence and flat field. Note that aside from $P_{L,\lambda}(x, y)$ and $A_{L,\lambda}(x, y)$, all other right-hand terms have no spatial dependency:

$$\frac{R \cdot R_{L,\lambda_2}(x, y) - R_{L,\lambda_1}(x, y)}{R - 1} = \frac{1}{\alpha} \cdot P_L(x, y) \tag{7}$$

$$\frac{R \cdot R_{L,\lambda_1}(x, y) - R \cdot R_{L,\lambda_2}(x, y)}{R - 1} = \frac{1}{\alpha} \cdot \left(A_L(x, y) \frac{Q_{A,\lambda_1}}{Q_{P,\lambda_1}} \right). \tag{8}$$

From combining Eqs. 4–8, we can obtain images representing the relative contribution of probe fluorescence to the total fluorescence at both wavelengths ($\%P_{L,\lambda}(x, y)$):

$$\begin{cases} \%P_{L,\lambda_1}(x, y) = 100 \cdot \left(R \cdot \dfrac{R_{L,\lambda_2}(x, y)}{R_{L,\lambda_1}(x, y)} - 1 \right) \Big/ (R - 1) \\ \%P_{L,\lambda_2}(x, y) = 100 \cdot \left(R - \dfrac{R_{L,\lambda_1}(x, y)}{R_{L,\lambda_2}(x, y)} \right) \Big/ (R - 1). \end{cases} \tag{9a,b}$$

A similar strategy in a different form has been published for reconstructing donor and acceptor images from a resonance energy transfer imaging problem (Ludwig et al., 1992).

RESULTS AND DISCUSSION

Synthesis and bioactivity of fluorescent Nod factor

To obtain a fluorescently labeled Nod factor, chitotetraose was deacetylated with NodB, and the free amino group was N-acylated with a C16 fatty acyl chain with a BODIPY FL tag. The structure of the fluorescent Nod factor (NodRlv-IV(BODIPY FL C_{16})) is shown in Fig. 1 *A*, and the reversed-phase HPLC profiles (Fig. 1, *B* and *C*) indicate its purity.

The newly synthesized Nod factor was tested in the root hair deformation assay with *Vicia sativa* (Heidstra et al., 1994). At a concentration of 10^{-6} M NodRlv-IV(BODIPY FL C_{16}), 60–80% of the susceptible zone hairs were de-

formed of all tested roots (n = 24) within 3 h. The deformation was confined to the susceptible zone, as is the case for natural Nod factors (Heidstra et al., 1994). At 10^{-8} M, 9 of 12 tested roots showed deformed hairs (only in the susceptible zone), although the number of deformed hairs was reduced. At 10^{-9} M no root hair deformation was detectable within 3 h (n = 12). Control (no Nod factor added) plants did not show deformation (n = 12). The new fluorescent Nod factor was also tested in the tobacco protoplast assay (Röhrig et al., 1995, 1996) and could induce protoplast division to an extent of 50% at concentrations equal to or higher than 10^{-9} M. At concentrations below 10^{-9} M, the number of dividing protoplasts gradually reduced (Röhrig, unpublished results). These experiments show that the synthesized fluorescent Nod factor is bioactive in different plant systems, implying that the presence of the BODIPY FL moiety does not abolish the biological activity. Natural Nod factors, however, are also bioactive at lower concentrations (Heidstra et al., 1994; Röhrig et al., 1995). Still, one can conclude that the structural demands for bioactivity at the end of the fatty acid tail of Nod factors are not very strict.

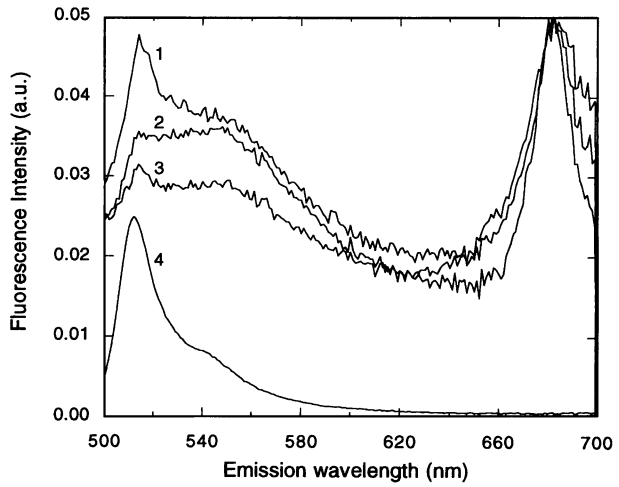

FIGURE 2 Fluorescence emission spectra of homogenized susceptible zones of *Vicia sativa* preincubated with various amounts of NodRlv-IV(BODIPY FL-C_{16}) (*1, 2, 3*) and of 33 nM NodRlv-IV(BODIPY FL-C_{16}) in Fåhraeus medium (*4*). *Vicia sativa* roots were labeled with 1 μM (*1*), 1 nM (*3*), or 0 nM (*2*) NodRlv-IV(BODIPY FL-C_{16}) in Fåhraeus medium as described. After 10 min the roots were washed three times with Fåhraeus medium, and the susceptible zones were cut out by a razor blade. The zones were frozen in liquid nitrogen and subsequently homogenized. After dissolving in 3 ml of Fåhraeus medium, the samples were used for fluorescence spectroscopy (for conditions see Materials and Methods).

Fluorescence spectroscopy

To investigate the fluorescent properties of the newly synthesized Nod factor, we measured fluorescence spectra of pure NodRlv-IV(BODIPY FL-C_{16}) in solution and of homogenates of labeled susceptible zones of *Vicia sativa* roots. For the latter, 12 roots (5 days after germination) were incubated with 0, 10^{-6}, or 10^{-9} M NodRlv-IV(BODIPY FL-C_{16}) for 10 min and washed three times with Fåhraeus medium, and the susceptible zones were cut out, homogenized, and resuspended in Fåhraeus medium. The results are shown in Fig. 2. The highly turbid homogenates exhibited strong autofluorescence, as is apparent from the control experiment, where the fluorescent labeling was omitted (*curve 2*). The autofluorescence spectrum showed two components: one with a broad emission band from 500 to 620 nm and one with a sharper peak from 660 to 700 nm. These bands most likely correspond to flavonoid and porphyrin autofluorescence (Guilbault, 1973; Tsien and Waggoner, 1990). When NodRlv-IV(BODIPY FL-C_{16}) was added at a concentration of 10^{-6} M, the fluorescence emission spectrum (*curve 1*) showed an increase in the range of BODIPY FL-fluorescence (compare *curves 1* and *4*). Such an increase was also seen at a labeling concentration of 10^{-9} M (*curve 3*), but was much less pronounced. It may be apparent from these spectra that the signal-to-noise (i.e., BODIPY-to-autofluorescence) ratio becomes very unfavorable at these low (but biologically more relevant) concentrations. By performing spectral fitting (according to Eq. 2 and omitting the spatial dimension x), using spectrum 1 or 3 as $S_L(\lambda)$ (instead of $S_L(\lambda,x)$), spectrum 2 as $S_A(\lambda)$, and spectrum 4 as $S_P(\lambda)$, we could determine that by labeling with 10^{-6} M and 10^{-9} M, 4.1 pmol and 0.47 pmol, respectively, were recovered from 12 susceptible zones. The spectral fitting was restricted to the fluorescence spectrum between 500 and 600 nm, and identical fluorescence quantum yields of NodRlv-IV(BODIPY FL-C_{16}) in Fåhraeus medium as compared to that bound to homogenized parts of susceptible zones in solution were assumed. The apparent binding efficiencies in the respective situations (0.2% and 24%) are clearly different, probably because of a saturation effect at the higher NodRlv-IV(BODIPY FL-C_{16}) concentration.

Fluorescence spectral imaging microscopy

With FSPIM it is possible to capture fluorescence emission spectra of a microscopic sample and retain spatial information. We applied this technique to study the labeled root system of *Vicia sativa*, with the aim of measuring fluorescence spectra of the in vivo system rather than of the homogenized samples as described above. In Fig. 3, two sizes of the entrance slit of the imaging spectrograph used are superimposed on a fluorescence micrograph of a root system (labeled for 10 min with 1 μM NodRlv-IV(BODIPY FL-C_{16} and washed). The fluorescence originating from the 50-μm (narrow) slit is passed on to a grating in the spectrograph, and the resulting image spectrum can be captured by a CCD camera. The distance-averaged spectra of the top half of the slit (the root hair area) and of the lower half of the slit (the root surface or epidermis area) and the central root area are shown in Fig. 4. In this figure, the distance-averaged spectra of 1 μM NodRlv-IV(BODIPY FL-C_{16}) in Fåhraeus medium and of an unlabeled root system are

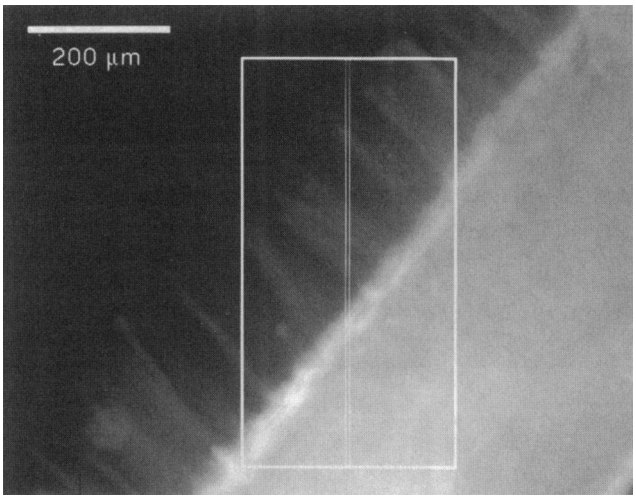

FIGURE 3 Entrance slit of the imaging spectrograph superimposed on a fluorescence micrograph of a *Vicia sativa* root labeled with NodRlv-IV(BODIPY FL-C_{16}). The large rectangle corresponds to the maximum slit width of 3 mm, whereas the smaller one shows the 50-μm slit width used in the experiment described in Fig. 4. The image was taken by a Photometrics CH220 camera placed on the other output port of the Axioplan microscope, enabling standard digital imaging (shown in this figure) and simultaneous spectral imaging (shown in Fig. 5). The CCD camera is described in detail elsewhere (Gadella and Jovin, 1995).

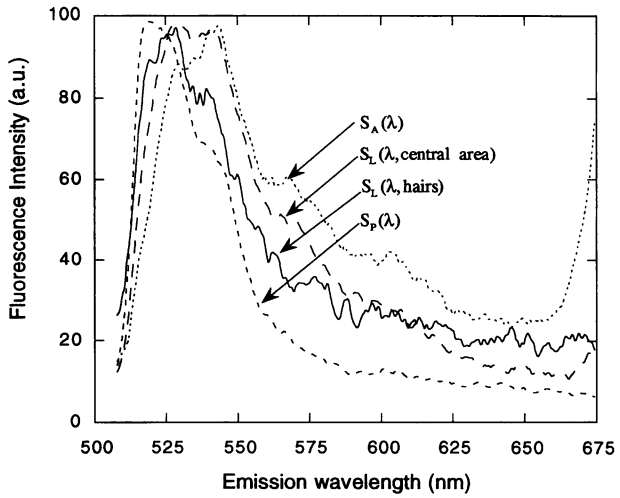

FIGURE 4 Distance-averaged image spectrums as obtained by FSPIM. Four samples were prepared on Fåhraeus slides: labeled roots (i), unlabeled roots (ii), a homogeneous solution of 1 μM NodRlv-IV(BODIPY FL-C_{16}) in Fåhraeus medium (iii), and a blank (Fåhraeus medium, iv). The labeled roots were incubated for 10 min with 1 μM NodRlv-IV(BODIPY FL-C_{16}) in Fåhraeus medium and subsequently washed three times with Fåhraeus medium. Image spectra were recorded as described in the experimental procedures section. The image spectrum (iv) was subtracted from (i), (ii), and (iii), yielding three background-corrected spectral images (i*) (= $S_L(\lambda, x)$), (ii*), and (iii*), respectively. The spectral images (ii*) and (iii*) were integrated along the spatial dimension to yield $S_A(\lambda)$ and $S_P(\lambda)$, respectively. Image spectrum (i) was taken from the slit as shown in Fig. 3. The top and lower halves were integrated separately along the vertical dimension to yield $S_L(\lambda$, hairs) and $S_L(\lambda$, central area), respectively, which correspond to the root hair and the epidermis + central areas. For representation purposes only, the spectra were smoothed using a uniform mask of 3.6 nm.

shown. The shape of the spectra differs from those presented in Fig. 1 because of 1) the presence of an emission longpass filter that reduced the fluorescence at wavelengths less than 520 nm; 2) the different instrument response characteristics of the imaging spectrograph-CCD camera detection system (which are not corrected for); and 3) the difference in sample preparation. The spectrum of NodRlv-IV(BODIPY FL-C_{16}) is clearly blue shifted with respect to the spectrum taken from unlabeled plants. The spectrum of the root hair area is more blue shifted than the spectrum taken from the central root and epidermis area, but both are positioned between the spectra of the unlabeled root system and that of pure NodRlv-IV(BODIPY FL-C_{16}). This indicates that NodRlv-IV(BODIPY FL-C_{16}) fluorescence is detected in both regions, but that the ratio of NodRlv-IV(BODIPY FL-C_{16}) fluorescence to autofluorescence is larger in the root hair area than in the rest of the root system.

Using the spectrum of NodRlv-IV(BODIPY FL-C_{16}) in Fig. 4 as $S_P(\lambda)$ and that of the unlabeled root system as $S_A(\lambda)$, one can apply Eq. 2 to break down the image spectrum of the labeled root system ($S_L(\lambda, x)$) into the autofluorescence image spectrum ($\alpha(x) \cdot S_A(\lambda)$) and the NodRlv-IV(BODIPY FL-C_{16}) image spectrum ($\beta(x) \cdot S_P(\lambda)$). Only the region between 500 and 600 nm of the spectrum was used for the calculation, thereby omitting the porphyrin-like fluorescence contribution, which was found to be spatially dependent, as it was specifically localized in the central area of the root (data not shown). The result is shown in Fig. 5. The vertical dimension of the images shown corresponds to the position along the small rectangle in Fig. 3, whereas the horizontal dimension is the fluorescence emission wavelength. The sum of the NodRlv-IV(BODIPY FL-C_{16}) image spectrum (Fig. 5 *D*) and the autofluorescence spectrum (Fig. 5 *E*) is shown in Fig. 5 *B*. The close resemblance of this fitted image spectrum (Fig. 5 *B*) with the original image spectrum (Fig. 5 *A*) is apparent and further demonstrated by the dark difference image spectrum (Fig. 5 *C*), which shows that the image spectrum of the labeled root system can indeed be described as a sum of an autofluorescence spectrum and a NodRlv-IV(BODIPY FL-C_{16}) spectrum. This indicates that upon binding of NodRlv-IV(BODIPY FL-C_{16}) to the root system, the BODIPY spectrum does not change. In Fig. 5 *F*, the percentage of NodRlv-IV(BODIPY FL-C_{16}) fluorescence is shown at each pixel in the image spectrum. From this image it is clear that in the region of 500–530 nm, this ratio is highest for all parts of the root system, as could be expected from the NodRlv-IV(BODIPY FL-C_{16}) spectrum in solution (see Fig. 4). It is also apparent from Fig. 5 *F* that especially in the root hair part of the image (top half), most of the fluorescence originates from NodRlv-IV(BODIPY FL-C_{16}). From Fig. 5 *D* it is inferred that in addition to the root hairs, the epidermis area also binds NodRlv-IV(BODIPY FL-C_{16}).

The spectral image fitting procedure described above is the first example known to us of a spectral image recon-

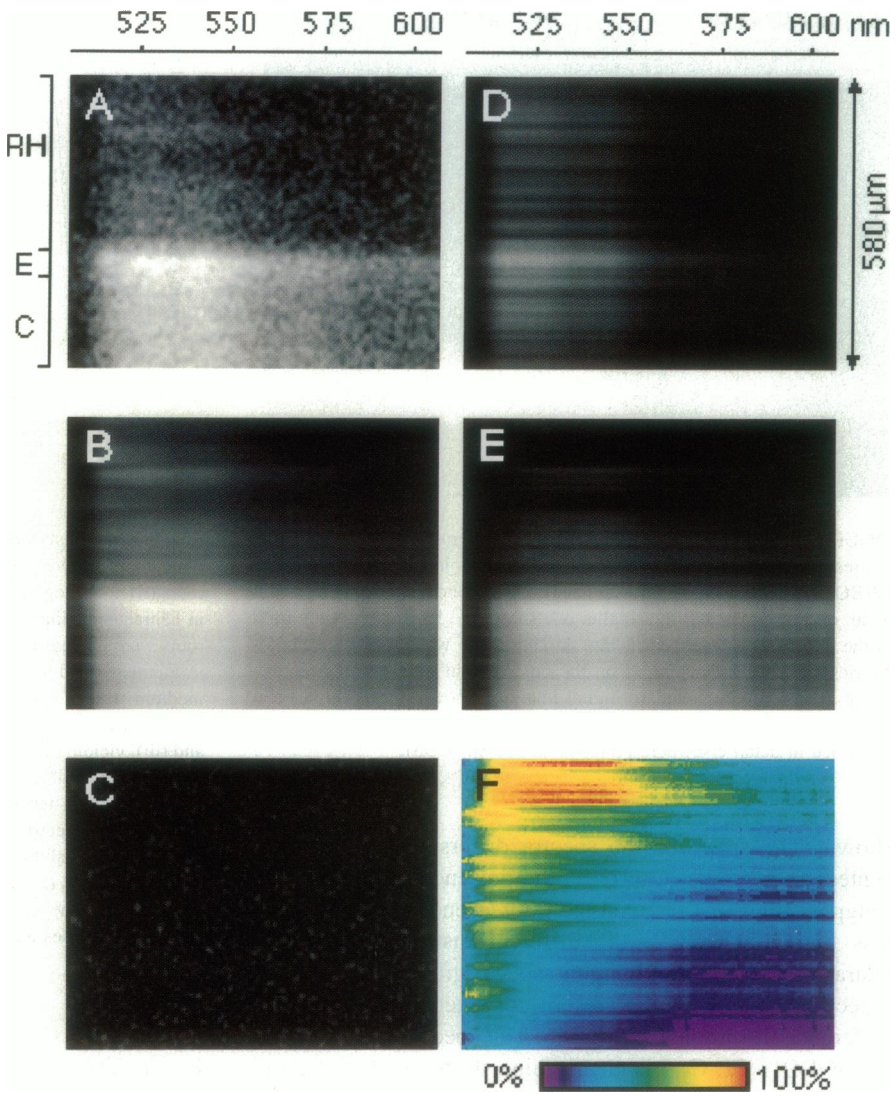

FIGURE 5 Autofluorescence correction by fluorescence spectral imaging microscopy of a NodRlv-IV(BODIPY FL-C_{16})-labeled living root of *Vicia sativa*. The spatial dimension (*vertical*) corresponds to the position along the narrow slit as shown in Fig. 3. The relative contributions of autofluorescence and probe fluorescence were calculated for $S_L(\lambda,x)$, using $S_A(\lambda)$ and $S_P(\lambda)$ as shown in Fig. 4 (see Eq. 2). The results of the fits are: (*A*) $S_L(\lambda,x)$ (observed); (*B*) $S_L(\lambda,x)$ (calculated, $= \alpha(x) \cdot S_A(\lambda) + \beta(x) \cdot S_P(\lambda)$); (*C*) abs(image *A* − image *B*); (*D*) $\beta(x) \cdot S_P(\lambda)$ (= NodRlv-IV(BODIPY FL-C_{16}) spectral image); (*E*) $(\alpha(x) \cdot S_A(\lambda)$ = autofluorescence spectral image); (*F*) 100 × image *D*/image *B*. The different root regions are indicated on image *A*: RH, root hair; E, epidermis; C, central zone.

struction into two individual image spectrum components. The fact it can be done accurately at all positions in the root system lends strong support to the concept that the shapes of both the autofluorescence and the NodRlv-IV(BODIPY FL-C_{16}) fluorescence emission spectra are indeed similar at all positions in the root system. This is an essential precondition for the fluorescence ratio imaging method for correcting autofluorescence in conventional fluorescence micrographs, as outlined below.

Fluorescence ratio imaging microscopy

The in situ localization of NodRlv-IV(BODIPY FL-C_{16}) binding sites on *Vicia sativa* roots was further studied by FRIM. As autofluorescence significantly contributes to the total fluorescence intensity in the images, one needs to correct for it. A simple procedure of measuring the difference in fluorescence intensity before and after addition of the fluorescent Nod factor, or measuring the decrease in fluorescence intensity after addition of an excess of unlabeled Nod factor is not possible, because the root hairs in the standard root hair deformation assay (Heidstra et al., 1994) are not immobilized, and hence no image arithmetic can be performed on the subsequent images. Moreover, comparing labeled and unlabeled roots will not work, as the autofluorescence intensity will differ from one root to another and, in addition, is spatially dependent within one root. Therefore we used a ratio imaging procedure as outlined above, to reconstruct the autofluorescence and the dye fluorescence in the image. The detection wavelengths were chosen on the basis of the ratio image spectrum (Fig. 5 *F*), indicating that at 525 nm a high BODIPY/autofluorescence ratio can be expected, whereas at 580 nm a low ratio can be expected. One vital prerequisite is that the ratio of autofluorescence intensities at the two wavelengths of detection is not spatially dependent. This was checked by acquiring images of an unlabeled root system at two emission wavelengths (525 nm and 580 nm) and rationing the respective

images. The image taken at 525 nm, corrected for flat-field and background fluorescence according to Eq. 4, is presented in Fig. 6 *A*. The ratio image *R*, representing a pixel-by-pixel division of the 525-nm and 580-nm flat-field- and background-corrected images, is shown in the pseudocolored Fig. 6 *B*. This image clearly demonstrates that the ratio of fluorescence intensities at the respective emission wavelengths is constant for the root system. The average value ± SD was found to be 0.16 ± 0.01 and was used in further image processing.

In Fig. 7, the results are shown for the autofluorescence correction of fluorescence micrographs taken from a labeled root system. The left column of images corresponds to detection at 525 nm, whereas images on the right correspond to detection at 580 nm. Images 7 *A* and 7 *E* represent the flat-field- and background-corrected images taken at the respective wavelengths. The reconstructed NodRlv-IV (BODIPY FL-C_{16}) fluorescence images are shown in Fig. 7, *B* and *F*. The autofluorescence (images 7 *C* and 7 *G*) is also present at both wavelengths, but constitutes most of the fluorescence intensity in the images taken at 580 nm. The relative amount of NodRlv-IV(BODIPY FL-C_{16}) fluorescence as compared to the total fluorescence is presented in the pseudocolored images 7 *D* and 7 *H* at the two wavelengths. From comparing Figs. 7 *D* and 7 *H*, it is apparent that this relative amount is clearly higher at 525 nm than at 580 nm. Furthermore, from Fig. 7 *D* it is inferred that NodRlv-IV(BODIPY FL-C_{16}) fluorescence constitutes about 80% of the total fluorescence in the root hairs, and this relative amount gradually decreases to about 20% in the central root area. This is in agreement with the ratio image spectrum as shown in Fig. 5 *F*. Most likely, the NodRlv-IV(BODIPY FL-C_{16}) fluorescence in the central area of the root originates from out-of-focus fluorescence from root hairs and epidermis cells above the plane of the detection. For this reason, it is hard to draw any conclusion about

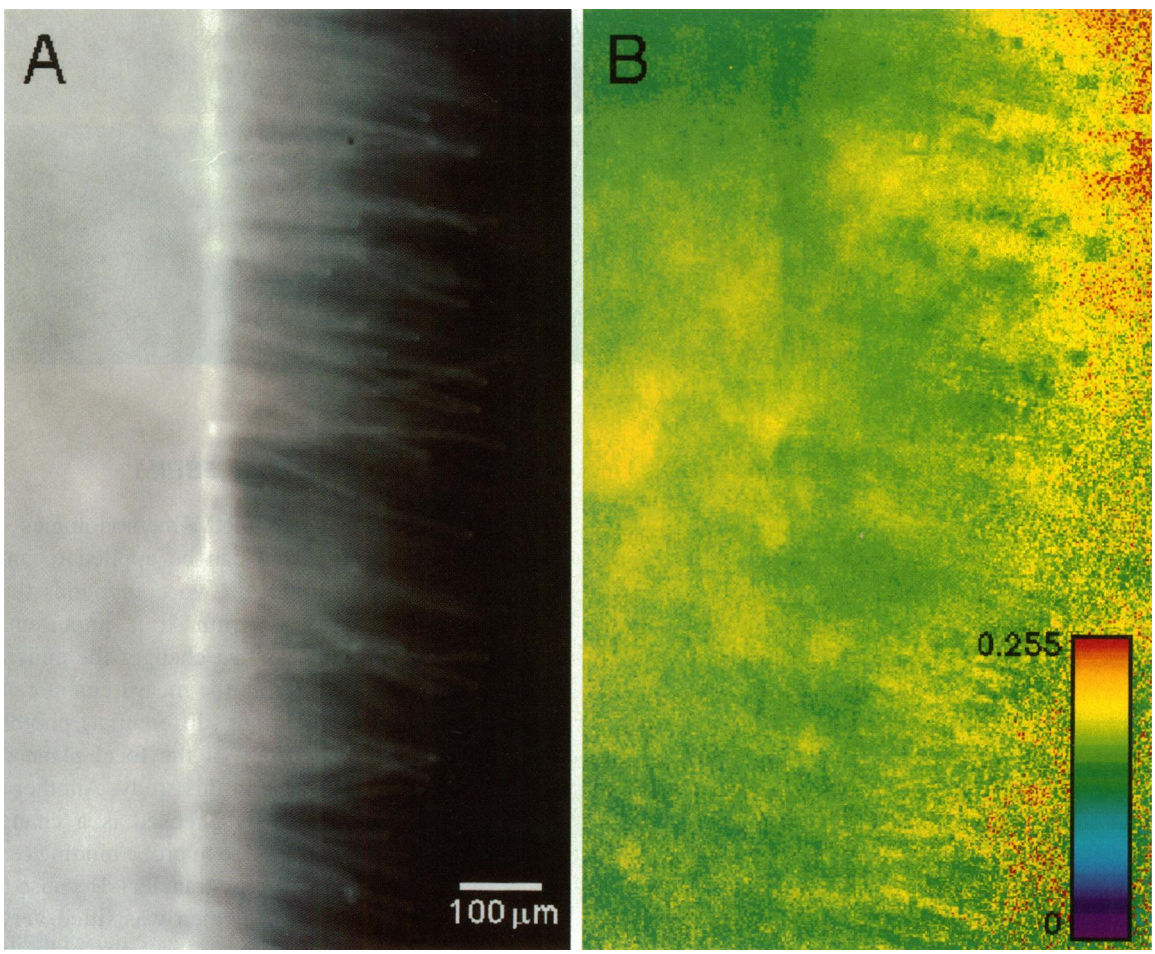

FIGURE 6 FRIM of autofluorescence originating from a living *Vicia sativa* root. Living *Vicia sativa* roots grown on microscope slides were used for fluorescence microscopy to yield $F_{U,\lambda}(x, y)$. Slides containing only Fåhraeus medium were used to image the background fluorescence ($F_{B,\lambda}(x, y)$). Two images were taken at two wavelengths of detection: either with a green filter (D525/20, λ_1) or with an orange filter (D580/40, λ_2). The images taken with the green filters were corrected for registration relative to those taken with the orange filter before further image processing (Waggoner et al., 1989). (*A*) The flat-field- and background-corrected image (Jericevic et al., 1989) $R_{U,\lambda 1}(x, y)$ (see Eq. 5); (*B*) the ratio image *R* according to Eq. 6. The average pixel value ± SD for the root area in this image is 0.16 ± 0.01. All image processing was done with IPLab for Macintosh PPC (Signal Analytics, Vienna, VA). Before image ratios were calculated, all images were converted to floating-point images.

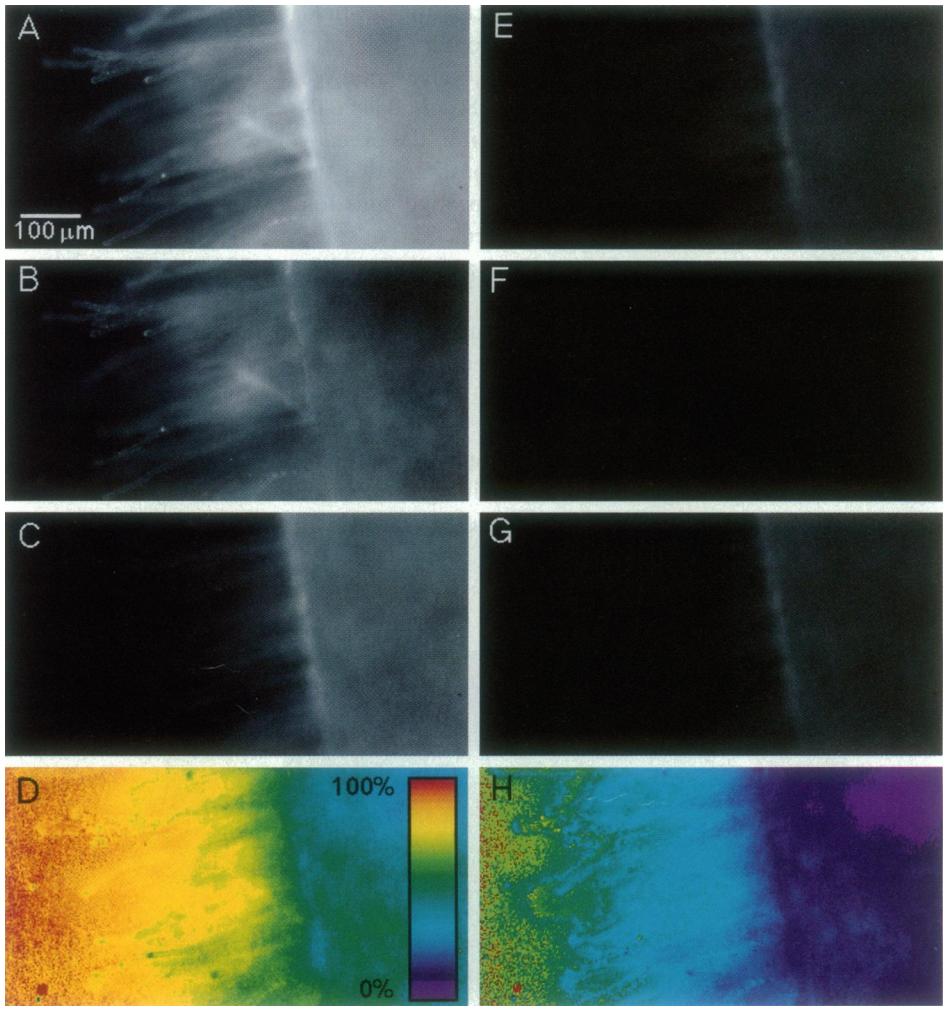

FIGURE 7 Autofluorescence correction by fluorescence digital imaging microscopy of a NodRlv-IV(BODIPY FL-C_{16})-labeled living root of *Vicia sativa*. Living *Vicia sativa* roots grown on a microscope slide were incubated with 1 μM NodRlv-IV(BODIPY FL-C_{16}) in Fåhraeus medium for 10 min. Subsequently, the roots were washed three times with Fåhraeus medium to remove unbound NodRlv-IV(BODIPY FL-C_{16}). The labeled root systems were used directly for fluorescence microscopy to yield $F_{L,\lambda}(x, y)$ images. The images were taken at two wavelengths: with a green filter (D525/20, λ_1) or an orange filter (D580/40, λ_2). The image taken with the green filter was corrected for registration relative to the image taken by the orange filter before going through the image-processing routine. The images $F_{P,\lambda}(x, y)$ and $F_{B,\lambda}(x, y)$ and the average ratio $R = 0.16$ described in Fig. 6 were used for the image processing. The images shown are $R_{L,\lambda1}(x, y)$ (*A*), $(1/\alpha) \cdot P_L(x, y)$ (*B*), $(1/\alpha) \cdot (A_L(x, y)(Q_{A,\lambda1}/Q_{P,\lambda1}))$ (*C*), $\%P_{L,\lambda1}(x, y)$ (*D*), $R_{L,\lambda2}(x, y)$ (*E*), $(1/\alpha) \cdot P_L(x, y)$ (*F*), $(1/\alpha) \cdot (A_L(x, y)(Q_{A,\lambda2}/Q_{P,\lambda2}))$ (*G*), and $\%P_{L,\lambda2}(x, y)$ (*H*) (see Eqs. 4 and 7–9). The images *E*–*G* were reduced 10.5-fold in intensity, so that the ratio of images *A* and *E* (i.e., $R_{L,\lambda1}(x, y)$ and $R_{L,\lambda2}(x, y)$) was similar to that observed in the microscope.

transport or localization of NodRlv-IV(BODIPY FL-C_{16}) in the interior parts of the root system from the data presented in Fig. 7 (and Fig. 5). It is of interest that the high fluorescence intensities at root hair tips that were in focus are visible in images 7 *A* and 7 *B* but not in image 7 *C*, and hence originate from NodRlv-IV(BODIPY FL-C_{16}). This shows that the Nod factor has a preference for the root hair tips, but also clearly indicates that the image reconstruction is done accurately: certain structures specifically correspond to the NodRlv-IV(BODIPY FL-C_{16}) signal. Furthermore, the epidermis area is clearly stained, indicating that all surface parts of the root system are stained with NodRlv-IV(BODIPY FL-C_{16}).

In a previous study, radioactive Nod factor was applied to a sectioned *Vicia sativa* root, and the distribution was studied by autoradiography (Heidstra et al., 1994). It was shown that Nod factors predominantly bind to root hairs, but also to epidermal cells. We confirm these earlier findings in the in vivo situation, but emphasize the much larger sensitivity and spatial resolution: one digital fluorescence micrograph (with a low power and low NA lens) is obtained within 5 s, whereas the autoradiography may take 2 weeks.

Comparison of FRIM and FSPIM

Both the FSPIM and the FRIM methodologies described here are very general and can be applied to any system exhibiting fluorescence from two compounds that have a different fluorescence spectrum. It is important to note, however, that any process that changes the emission spectrum of the specimen during the measurement can produce misleading results. Therefore (differential) photobleaching and wavelength dependency of the focal plane should be negligible, as was the case in this study. Another source of errors that cannot be easily checked is a change in the autofluorescence spectrum due to probe binding (e.g., due to fluorescence resonance energy transfer). Because the image spectrum of the labeled specimen was fitted very well by using only two components, it is very unlikely that in experiments described here the autofluorescence spectrum was changed because of NodRlv-IV(BODIPY FL-C_{16}) binding.

An obvious advantage of the FRIM procedure over the FSPIM procedure is that a true two-dimensional image is obtained of the probe distribution. On the other hand, ra-

tioning of fluorescence emission images (as described here) is sensitive to registration problems due to differences in the positioning and size of the emission filters, which require additional corrections. In the image spectrograph, the image spectra are obtained in one exposure, making this method insensitive to registration problems. Another big advantage of FSPIM is that a true least-squares fitting of all of the data along the spectroscopic axis of the image spectrum is performed, reducing the sensitivity toward noise, whereas the FRIM method evaluates only two spectral points with concomitant consequences for the noise sensitivity. Even when the autofluorescence spectrum is spatially dependent because of two autofluorescing components that are differentially distributed in the specimen, the FSPIM procedure can, in principle, correct for the autofluorescence. A precondition is that the fluorescence spectra of the individual components are known and that they are different from the probe fluorescence spectrum. In this case one can simply extend Eq. 1 by adding a third component (e.g., $\gamma(x) \cdot S_{A2}(\lambda)$), which leads to a 3×3 inverted matrix procedure in the subsequent linear least-squares fit of the spatial contribution factors. The FRIM procedure, on the other hand, will suffer from an accumulation of noise problems: one must acquire images of the four samples at three different wavelengths and then perform a triple rationing procedure.

CONCLUDING REMARKS

We have described the synthesis of NodRlv-IV(BODIPY FL-C_{16}), which is the first bioactive and fluorescent Nod factor known to us. We have demonstrated its use for localizing Nod factor-binding sites on living *Vicia sativa* roots. A novel spectral image fitting procedure and a fluorescence ratio imaging technique are introduced to effectively correct for autofluorescence of the root system (inherent to many plant systems). After these corrections, we could show that the fluorescent Nod factor analog predominantly binds to the root hairs and root epidermis, and that there is an increased labeling in the root hair tips. This shows that an autofluorescing plant system can also be used for fluorescence labeling studies. However, a system with low autofluorescence in the spectral range of the probe is preferable.

Because root autofluorescence is decreased to a great extent by using higher excitation wavelengths (Gadella, unpublished results), we have undertaken the effort of synthesizing another fluorescent Nod factor containing a different BODIPY-labeled acyl chain (BODIPY 581/591-C_{12}). This Nod factor analog has favorable fluorescence properties as compared to NodRlv-IV(BODIPY FL-C_{16}), because it can be imaged in the near-absence of autofluorescence. Its in situ distribution confirmed the in situ distribution of NodRlv-IV(BODIPY FL-C_{16}) (Gadella, unpublished results), which validates the autofluorescence correction methodology described here. However, unfortunately, this Nod factor was found to be biologically inactive in the root hair deformation assay. We are currently investigating for bioactivity Nod factors containing other BODIPY fatty acyl chains that also exhibit red-shifted spectral properties. We expect that those red-shifted dyes, in combination with the digital imaging techniques described here, will enable us to study the microenvironment of the Nod factor-binding site in vivo, and hence shed new light on the putative Nod factor receptor and its downstream signal transduction cascade.

The collaboration between TWJG and GV was supported by a NATO collaborative research grant (TWJG and Dr. T. M. Jovin (MPIBPC)). TWJG was supported by the Netherlands Foundation for Scientific Research (NWO) and by the Royal Netherlands Academy of Sciences (KNAW). GV was the recipient of a postdoctoral grant from the Alexander von Humboldt Foundation and was supported by OTKA grant F013335. TB and J. Schmidt were supported by grants from the European Union.

REFERENCES

Aikens, R. S., D. A. Agard, and J. W. Sedat. 1989. Solid-state imagers for microscopy. *In* Fluorescence Microscopy of Living Cells in Culture, Part A. Fluorescent Analogs, Labelling Cells, and Basic Microscopy. Y.-L. Wang and D. L. Taylor, editors. Academic Press, San Diego. 291–313.

Arndt-Jovin, D. J., S. A. Latt, G. Striker, and T. M. Jovin. 1979. Fluorescence decay analysis in solution and in a microscope of DNAs and chromosomes stained with quinacrine. *J. Histochem. Cytochem.* 27: 87–95.

Balaban, R. S., I. Kurtz, H. E. Cascio, and P. D. Smith 1985. Microscopic spectral imaging using a video camera. *J. Microsc.* 141:31–39.

Beach, D. A., K. S. Wells, F. Husher, and C. Bustamante 1987. Differential polarization microscope using an image dissector camera and phase-lock detection. *Rev. Sci. Instrum.* 58:1987–1995.

Beverloo, H. B., A. van Schadewijk, J. Bonnet, R. vad der Geest, R. Runia, N. P. Verwoerd, J. Vrolijk, J. S. Ploem, and H. J. Tanke 1992. Preparation and microscopic visualization of multicolor luminescent immunophores. *Cytometry.* 13:561–570.

Bhuvaneswari, T. V., and B. Solheim 1985. Root hair deformation in the white clover/*Rhizobium trifolii* symbiosis. *Physiol. Plant.* 63:25–34.

Bright, G. R., G. W. Fisher, J. Rogowska, and D. L. Taylor. 1989. Fluorescence ratio imaging microscopy. *In* Fluorescence Microscopy of Living Cells in Culture, Part B. Quantitative Fluorescence Microscopy—Imaging and Spectroscopy. D. L. Taylor and Y.-L. Wang, editors. Academic Press, San Diego. 157–190.

Burghardt, T. P., and K. Ajtai. 1991. Fluorescence polarization from oriented systems. *In* Topics in Fluorescence Spectroscopy. Vol. 2: Principles. J. R. Lakowicz, editor. Plenum Press, New York. 307–343.

Buurman, E. P., R. Sanders, A. Draaijer, H. C. Gerritsen, J. J. F. van Deen, P. M. Houpt, and Y. K. Levine 1992. Fluorescence lifetime imaging using a confocal laser scanning microscope. *Scanning.* 14:155–159.

Dénarié, J., and J. Cullimore 1993. Lipo-oligosaccharide nodulation factors: a new class of signalling molecules mediating recognition and morphogenesis. *Cell.* 74:951–954.

Divecha, N., and R. F. Irvine 1995. Phospholipid signalling. *Cell.* 80: 269–278.

Dix, J. A., and A. S. Verkman 1990. Mapping of fluorescence anisotropy in living cells by ratio imaging. *Biophys. J.* 57:231–240.

Draper, N., and H. Smith. 1981. Applied Regression Analysis. John Wiley and Sons, New York.

Ehrhardt, D. W., R. Wais, and S. R. Long 1996. Calcium spiking in plant root hairs responding to Rhizobium nodulation signals. *Cell.* 85: 673–681.

Fåhraeus, G. 1957. The infection of clover root hairs by nodule bacteria studied by a simple glass technique. *J. Gen. Microbiol.* 16:374–381.

Fisher, R. F., and S. R. Long. 1992. *Rhizobium*-plant induced signal exchange. *Nature.* 357:655–660.

Florine-Casteel, K., J. J. Lemasters, and B. Herman. 1990. Digitized fluorescence polarization microscopy of DPH and related probes in cell-size vesocles composed of gel- or fluid-phase phospholipid. *In* Optical Microscopy for Biology: Proceedings of the International Conference on Video Microscopy, June 4–7, 1989. B. Herman and K. Jacobson, editors. Wiley-Liss, New York. 559–574.

Gadella, T. W. J., Jr., and T. M. Jovin. 1995. Oligomerization of epidermal growth factor receptors (EGFR) on A431 cells studied by time-resolved fluorescence imaging microscopy. A stereochemical model for tyrosine kinase receptor activation. *J. Cell Biol.* 129:1543–1558.

Gadella, T. W. J., Jr., T. M. Jovin, and R. M. Clegg. 1993. Fluorescence lifetime imaging microscopy (FLIM): spatial resolution of microstructures on the nanosecond time scale. *Biophys. Chem.* 48:221–239.

Giuliano, K. A., M. A. Nederlof, R. DeBasasio, L. Frederick, A. S. Waggoner, and D. L. Taylor. 1990. Multi-mode light microscopy. *In* Optical Microscopy for Biology: Proceedings of the International Conference on Video Microscopy, June 4–7, 1989. B. Herman and K. Jacobson, editors. Wiley-Liss, New York. 543–558.

Guilbault, G. G. 1973. Practical Fluorescence. Theory, Methods, and Techniques. New York, Marcel Dekker.

Heidstra, R., and T. Bisseling. 1996. Nod factor-induced host responses and mechanisms of Nod factor perception. *New Phytol.* 133:25–43.

Heidstra, R., R. Geurts, H. Franssen, H. Spaink, A. van Kammen, and T. Bisseling. 1994. Root hair deformation activity of nodulation factors and the fate on *Vicia sativa*. *Plant Physiol.* 105:787–797.

Herman, B. 1989. Resonance energy transfer microscopy. *In* Fluorescence Microscopy of Living Cells in Culture, Part B. Quantitative Fluorescence Microscopy—Imaging and Spectroscopy. D. L. Taylor and Y.-L. Wang, editors. Academic Press, San Diego. 219–243.

Herman, B., and K. Jacobson, editors. 1990. Optical Microscopy for Biology. Wiley-Liss, New York.

Jericevic, Z., B. Wiese, J. Bryan, and L. C. Smith. 1989. Validation of an imaging system: steps to evaluate and validate a microscope imaging system for quantitative studies. *In* Fluorescence Microscopy of Living Cells in Culture, Part B. Quantitative Fluorescence Microscopy—Imaging and Spectroscopy. D. L. Taylor and Y.-L. Wang, editors. Academic Press, San Diego. 47–83.

John, M., H. Röhrig, J. Schmidt, U. Wieneke, and J. Schell. 1993. Rhizobium NodB protein involved in nodulation signal synthesis is a chitooligosaccaride deacetylase. *Proc. Natl. Acad. Sci. USA.* 90:625–629.

Jovin, T. M., and D. J. Arndt-Jovin. 1989a. FRET microscopy: digital imaging of fluorescence resonance energy transfer. Application in cell biology. *In* Cell Structure and Function by Microspectrofluorometry. E. Kohen and J. G. Hirschberg, editors. Academic Press, New York. 99–117.

Jovin, T. M., and D. J. Arndt-Jovin. 1989b. Luminescence digital imaging microscopy. *Annu. Rev. Biophys. Chem.* 18:271–308.

Jovin, T. M., D. J. Arndt-Jovin, G. Marriott, R. M. Clegg, M. Robert-Nicoud, and T. Schormann. 1990. Distance, wavelength and time: the versatile 3rd dimensions in light emission microscopy. *In* Optical Microscopy for Biology. B. Herman and K. Jacobson, editors. Wiley-Liss, New York. 575–602.

Kim, M. H., L. Ulibarri, and C. Bustamante. 1987. Differential polarization imaging. II. Symmetry properties and calculations. *Biophys. J.* 52: 929–946.

Lakowicz, J. R. 1994. Fluorescence lifetime imaging microscopy: homodyne technique using high-speed gated image intensifier. *Methods Enzymol.* 240:723–748.

Ludwig, M., N. F. Hensel, and R. J. Hartzman. 1992. Calibration of a resonance energy transfer imaging system. *Biophys. J.* 61:845–857.

Marriott, G., R. M. Clegg, D. J. Arndt-Jovin, and T. M. Jovin. 1991. Time-resolved imaging microscopy. Phosphorescence and delayed fluorescence imaging. *Biophys. J.* 60:1374–1387.

Marriott, G., M. Heidecker, E. P. Diamandis, and Y. Yan-Marriott. 1994. Time-resolved delayed luminescence imaging microscopy using a europium ion chelate complex. *Biophys. J.* 67:957–965.

Martinez-Zaguilan, R., L. S. Tomkins, and R. M. Lynch. 1994. Simultaneous analysis of multiple fluorescent probes in single cells by microspectroscopic imaging. *Proc. SPIE.* 2137:17–28.

Mickols, W. E., M. F. Maestre, J. I. Tinoco, and S. H. Embury. 1985. Visualization of oriented hemoglobin S in individual erythrocytes by differential extinction of polarized light. *Proc. Natl. Acad. Sci. USA.* 82:6527–6531.

Mylona, P., M. Moerman, B. C. Yang, T. Gloudemans, v. d. Kerckhove, A. van Kammen, T. Bisseling, and H. Franssen. 1994. The root epidermis of specific pea gene RH2 is homologous to a pathogen related gene. *Plant Mol. Biol.* 26:39–50.

Nap, J.-P., and T. Bisseling. 1990. Developmental biology of a plant-prokaryote symbiosis: the legume root nodule. *Science.* 250:948–954.

Nicolaou, K. C., N. J. Bockovich, D. R. Carnague, C. W. Hummel, and L. F. Even. 1992. Total synthesis of the NodRm-IV factors, the Rhizobium nodulation signals. *J. Am. Chem. Soc.* 114:8701–8702.

Röhrig, H., J. Schmidt, R. Walden, I. Czaja, H. Lubenow, U. Wieneke, J. Schell, and M. John. 1996. Convergent pathways for lipochitooligosaccharide and auxin signaling in tobacco cells. *Proc. Natl. Acad. Sci. USA.* 93:13389–13392.

Röhrig, H., J. Schmidt, R. Walden, I. Czaja, E. Miklashevics, U. Wieneke, J. Schell, and M. John. 1995. Growth of tobacco protoplasts stimulated by synthetic lipo-chitosaccharides. *Science.* 269:841–843.

Röhrig, H., J. Schmidt, U. Wieneke, E. Kondorosi, I. Barlier, J. Schell, and M. John. 1994. Biosynthesis of lipooligosaccharide nodulation factors: *Rhizobium* NodA protein is involved in N-acylation of the chitooligosaccharide backbone. *Proc. Natl. Acad. Sci. USA.* 91:3122–3126.

Spaink, H. P. 1992. Rhizobial lipo-olichosaccharides: answers and questions. *Plant Mol. Biol.* 20:977–986.

Trepte, O., I. Rokahr, S. Andersson-Engels, and K. Carlsson. 1994. Studies of porphyrin-containing specimens using an optical spectrometer connected to a confocal scanning laser microscope. *J. Microsc.* 176: 238–244.

Tsien, R. Y., and A. Waggoner. 1990. Fluorophores for confocal microscopy: photophysics and photochemistry. *In* Handbook of Biological Confocal Microscopy. J. B. Pawley, editor. Plenum Press, New York. 169–178.

Van Brussel, A. A. N., S. A. J. Zaat, H. C. J. Canter Cremers, C. A. Wijffelman, E. Pees, T. Tak, and B. J. J. Lugtenberg. 1982. Small leguminosae as test plants for nodulation of *Rhizobium leguminosarum* and other rhizobia and agrobacteria harbouring a leguminosarum Symplasmid. *Plant Sci. Lett.* 27:317–325.

Vijn, I., F. Martinez-Abarca, Y. W.-C. L. das Neves, A. van Brussel, A. van Kammen, and T. Bisseling. 1995. Early nodulin gene expression during Nod factor induced processes in *Vicia Sativa*. *Plant J.* 8:111–119.

Waggoner, A., R. DeBiasio, P. Conrad, G. R. Bright, L. Ernst, K. Ryan, M. Nederlof, and R. D. Taylor. 1989. Multiple spectral parameter imaging. *In* Fluorescence Microscopy of Living Cells in Culture, Part B. Quantitative Fluorescence Microscopy—Imaging and Spectroscopy. D. L. Taylor and Y.-L. Wang, editors. Academic Press, San Diego. 449–476.